Available online at www.sciencedirect.com
SCIENCE DIRECT®
Thin Solid Films 455–456 (2004) 571–575
thin solid films
www.elsevier.com/locate/tsf

# Analysis of the optical properties and structure of sculptured thin films from spectroscopic Mueller matrix ellipsometry

N.J. Podraza, Chi Chen, Ilsin An, G.M. Ferreira, P.I. Rovira, R. Messier, R.W. Collins*

*Department of Physics and Materials Research Institute, The Pennsylvania State University, University Park, PA 16802, USA*

**Abstract**

The Mueller matrices describing oblique incidence reflection and normal incidence transmission have been measured for sculptured thin films (STFs) by glancing angle deposition with simultaneous substrate rotation. In data reduction, the 15 parameters of the (1,1)-normalized real Mueller matrix are converted to the six parameters of the (2,2)-normalized complex Jones matrix. Two computational methods yield excellent agreement in the real and imaginary parts of the complex amplitude ratios $\rho_{ps}$ and $\rho_{sp}$ obtained in reflection (or $\tau_{ps}$ and $\tau_{sp}$ obtained in transmission). Multilayer optical analysis has been developed that employs step-wise variations of the principal axis Euler angles, associated with the local uniaxial structure in successive sublayers, in order to simulate variations in the column orientation with depth into the film. Such analysis has elucidated the Bragg resonance characteristics exhibited by the optical rotation of chiral STFs.


*Keywords:* Anisotropic thin films; Sculptured thin films; Chiral thin films; Spectroscopic Mueller matrix ellipsometry; Form birefringence; Optical rotation

## 1. Introduction

Sculptured thin films (STFs) can be prepared by physical vapor deposition (PVD) at glancing angle with simultaneous substrate rotation and source flux directional control [1]. The PVD conditions are chosen to ensure a well-defined columnar morphology. Fig. 1 shows the deposition geometry along with the angles $\Phi$ and $\Theta$ that define the source flux direction with respect to a coordinate system $(x, y, z)$ fixed in the substrate (where $z$ is normal to the surface). The columns in the film are azimuthally aligned in the flux direction, and a well-defined relationship, e.g. the tangent rule [2], is often found between the flux angle $\Theta$ and the polar column angle $\theta$ (measured with respect to the $z$ axis and serving as one of two Euler angles that define the local film structure). Thus, by varying $\Phi$ and $\Theta$ vs. time during deposition, one can 'sculpt' novel morphologies with tailored optical anisotropies.

In this report, we describe the first application of high speed Mueller matrix ellipsometry in reflection and transmission to characterize non-absorbing STFs. The measured Mueller matrix is converted to complex amplitude reflection or transmission ratios that are fit using an optical model. In this model, the orientation of the principal axis coordinate system $(x', y', z')$ of the locally uniaxial film structure is described by its azimuthal and polar Euler angles $(\phi, \theta)$ with respect to the $(x, y, z)$ system of the substrate and incident wave. A continuous evolution of the column direction with film depth can be approximated using a multilayer stack with stepwise variation in the Euler angles from one sublayer to the next. From this modeling, we can determine the film structure, including the thicknesses, void volume fractions, and Euler angles, as well as the film optical properties, including spectra of the average of the principal refractive indices $n_{av}=(1/2)(n_{x'}+n_{z'})$ and of the birefringence $\Delta n=n_{z'}-n_{x'}$. The importance of a direct measurement of the full spectroscopic Mueller matrix is also emphasized. This matrix can be applied to determine the response of the STF to any incident wavelength and polarization state, provided that one uses the same optical configuration as that in which the matrix is measured.

## 2. Experimental details

Two types of STFs prepared by electron beam evap-

*Corresponding author. Tel.: +1-814-865-3059; fax: +1-814-865-2326.
*E-mail address:* rwc6@psu.edu (R.W. Collins).

0040-6090/04/$ - see front matter © 2003 Elsevier B.V. All rights reserved.
doi:10.1016/j.tsf.2003.11.219

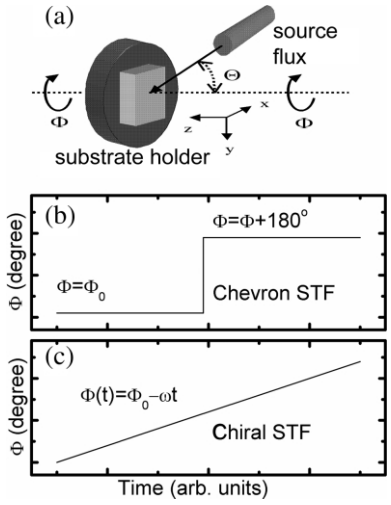


Fig. 1. (a) The geometry, and (b) and (c) azimuthal angular variations with time used for chevron and chiral STF fabrication by glancing angle deposition.

oration have been investigated as shown in Fig. 1. The first film is a $Ta_2O_5$ chevron STF, so named because of the film morphology observed in cross-section by scanning electron microscopy (SEM) [3]. This STF is prepared to a thickness $d \sim 2.7$ μm with a single $\Delta\Phi = 180°$ step halfway through the deposition. The second film is a $MgF_2$ chiral STF prepared to a thickness $d \sim 4.7$ μm with continuous substrate rotation $\Phi(t) = \Phi_0 - \omega t$ [4]. In this case, 12.3 clockwise substrate rotations yield a right-handed helicoidal morphology (counter-clockwise rotation of $\phi$ in progression from the substrate to the surface).

These STFs have been studied using a dual rotating-compensator multichannel ellipsometer. In this instrument, $MgF_2$ biplate compensators, before and after the sample, rotate synchronously at $5\omega$ and $3\omega$, where $\omega/2\pi = 2$ Hz [5,6]. The linear photodiode array detector is read 36 times per optical period $\pi/\omega = 0.25$ s. From these 36 integrations, one can determine spectra in the 25 non-zero d.c. and d.c.-normalized $[\cos(2n\omega t), \sin(2n\omega t)]$ Fourier coefficients $\{I_0, [\alpha_{2n}', \beta_{2n}']; n = 1,..., 8, 10, 11, 13, 16\}$ of the detected irradiance. Expressions have been reported that describe all 16 Mueller matrix elements in terms of the 25 coefficients and the instrument calibration data, which includes the polarizer and analyzer offset angles ($P_S$, $A_S$), the spectra in the compensators' phase angle ($C_{S1}$, $C_{S2}$) and retardance ($\delta_1$, $\delta_2$), and the spectral response function $I_{00}$ [5].

The experimental reflection ratios $\rho_{pp} \equiv r_{pp}/r_{ss} = \tan\psi_{pp}\exp(i\Delta_{pp})$, $\rho_{ps} \equiv r_{ps}/r_{ss} = \tan\psi_{ps}\exp(i\Delta_{ps})$, and $\rho_{sp} \equiv r_{sp}/r_{ss} = \tan\psi_{sp}\exp(i\Delta_{sp})$ (or the similarly-defined transmission ratios $\tau_{pp}$, $\tau_{ps}$, and $\tau_{sp}$) to be used in modeling are obtained by inverting the equation [7]:

$$\mathbf{M} = p\mathbf{A}\cdot(\mathbf{J}\otimes\mathbf{J}^*)\cdot\mathbf{A}^{-1} + (1-p)\mathbf{M}_D, \quad (1)$$

where **M** is the measured Mueller matrix, **J** is the deduced Jones matrix, and **A** is the 4×4 conversion matrix [8]. The second term includes the possibility of random depolarization, where $1-p$ describes the fraction of reflected (or transmitted) flux that is depolarized and $\mathbf{M}_D$ is the Mueller matrix for a perfect depolarizer. [$(\mathbf{M}_D)_{11} = \mathbf{M}_{11}$; otherwise $(\mathbf{M}_D)_{ij} = 0$.] This term can simulate the collection of multiply-scattered light from the sample [9] or stray light in the detector [10] and serves to improve Mueller–Jones conversion consistency. Because 15 (1,1)-normalized Mueller matrix elements are available, whereas seven parameters are obtained in the Eq. (1) inversion, there are different ways to obtain the three complex amplitude ratios. Elsewhere we have provided two equations for $\rho_{ps}$ and $\rho_{sp}$ and one equation each for $\rho_{pp}$, $|\rho_{pp}|^2$, $|\rho_{ps}|^2$, $|\rho_{sp}|^2$, and $p$, a total of 14 of 15 possible equations [11] (Analogous expressions are available for $\tau$).

## 3. Results and discussion

### 3.1. Chevron STF

Fig. 2 shows representative results for the two ways of determining the spectrum in the real part of $\rho_{sp}$ as measured for the $Ta_2O_5$ chevron STF in reflection at an incidence angle of $\theta_i = 70.20° \pm 0.05°$. Evidently, the film is optically anisotropic since $\rho_{sp}$ should vanish otherwise. The result designated $\rho_{sp}^{re}$ (solid line) is obtained from the upper right 2×2 Mueller matrix block (URB) with an upper-left-block (ULB) normalization, whereas the result designated $\rho_{sp1}^{re}$ (points) is obtained by combining the 2×2 lower left block (LLB) and lower right block (LRB), but with a different ULB normalization [11]. The agreement between the two spectra is very good, with the largest deviations occurring near the $Ta_2O_5$ interband onset where the anisotropy is sup-

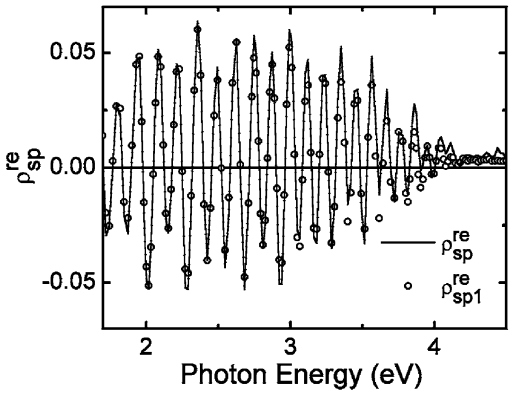


Fig. 2. Real part of $\rho_{sp}$ obtained experimentally for the chevron STF and computed from the 2×2 Mueller matrix URB ($\rho_{sp}^{re}$: line) and from the LLB and LRB ($\rho_{sp1}^{re}$: points). Two different ULB normalizations were required in these computations.

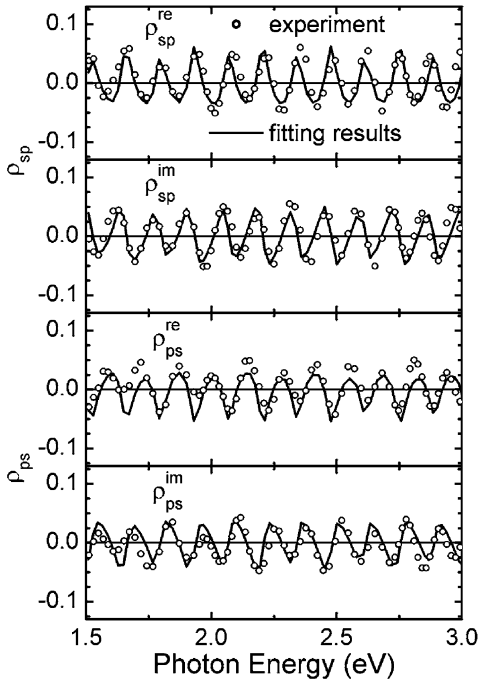


Fig. 3. Spectra in the real and imaginary parts of $\rho_{sp}$ and $\rho_{ps}$ for the chevron STF obtained experimentally and from a best-fit using a two-layer anisotropic model for the film.

pressed. Typically, the amplitude ratios obtained by different methods exhibit differences in ($\psi_{pp}$, $\psi_{ps}$, $\psi_{sp}$) of no more than 0.05°, demonstrating the consistency of the Mueller matrix with Eq. (1) [10]. For the STFs, such differences are sometimes larger due to the high frequency fringe patterns and depolarization that is inadequately modeled with a single parameter.

Fig. 3 shows experimental data in $\rho_{ps}$ and $\rho_{sp}$ (points) for the chevron STF over the range where the film is non-absorbing. The best fits (lines) adopt a two-layer model yielding microstructural and optical information via an initial grid search and least squares regression.

The deduced microstructural information includes the thicknesses and Euler angles for the top and bottom layers of the film ($d_1$, $\phi_1$, $\theta_1$) and ($d_2$, $\phi_2$, $\theta_2$), respectively. The polar angles are assumed to be identical for both layers ($\theta_1 = \theta_2$). In the Euler angle definitions, the rotations transform the 'unprimed' or substrate/wave coordinate system into the 'primed' or principal axis system of each columnar film. Here $z$ points into the substrate perpendicular to its surface and $z'$ points into the film parallel to its columns. Thus, $\theta$ is the angle directed from $z$ to $z'$, and $\phi_i$ is the angle directed from $x$ (i.e. the axis of intersection of the plane of incidence with the sample surface) to $x'$ (i.e. the axis in the surface plane orthogonal to the projection of the column axis in this plane). Best-fit parameters include ($d_1$, $\phi_1$) = (1.308 μm, 75°), ($d_2$, $\phi_2$) = (1.335 μm, 255°), and $\theta = 30°$ (lines in Fig. 3).

Optical information can also be deduced in the fit of Fig. 3. A Sellmeier form for the dielectric function $\varepsilon_b$ of the $Ta_2O_5$ columns is assumed, given by $\varepsilon_b(E) - \varepsilon_\infty = A^2/(E_0^2 - E^2)$. The principal dielectric function components are then given by the following two effective medium theory limits: $\varepsilon_{z'} = (1 - f_v)\varepsilon_b + f_v$, for no screening (electric fields parallel to the boundaries), and $(\varepsilon_{x'})^{-1} = (1 - f_v)(\varepsilon_b)^{-1} + f_v$, for maximum screening (fields perpendicular to the boundaries) [12]. With this model, the best-fit Sellmeier parameters are ($\varepsilon_\infty$, $E_0$, $A$) = (3.966, 3.136 eV, 0.476 eV) and the best-fit void volume fraction is $f_v = 0.034$. A birefringence of $\Delta n = n_{z'} - n_{x'} = 0.069$ is obtained in the limit of low frequencies. This is the key parameter to be maximized for applications of the films in polarization-modifying devices [3].

The best-fit parameters for the chevron STF are found to be in good agreement with expectations based on the fabrication procedure as well as with SEM images. First, the thicknesses of the two layers agree within 2%, consistent with the single substrate rotation after one-half the deposition time has elapsed. In addition, the difference in azimuthal Euler angles for the two layers is $\Delta\phi = \phi_2 - \phi_1 = 180°$, matching $\Delta\Phi$ used in fabrication. Estimates from the SEM images (at a different region of the film than that measured optically) yield thicknesses of $d_1 = 1.313$ μm and $d_2 = 1.374$ μm, and polar Euler angles of $\theta_1 \sim \theta_2 \sim 35°$, in reasonable agreement with the best-fit values. Perhaps the most critical assumption in the analysis of such films is that of the two-layer model. It is expected that such films exhibit void gradients and surface roughness, and these should be incorporated for improved results.

### 3.2. Chiral STF

Fig. 4 shows results for the two ways of determining $|\tau_{pp}|^2$ from the Mueller matrix for the $MgF_2$ chiral STF measured in transmission at normal incidence. Evidently, the film is anisotropic since this spectrum deviates from unity. The result in Fig. 4 designated $|\tau_{pp}|^2$ (closed circles) is obtained via $\tau_{pp}^{re}$ and $\tau_{pp}^{im}$ from the Mueller matrix LRB with ULB normalization, whereas the result designated $|\tau_{pp1}|^2$ (open circles) is obtained directly from the ULB alone [11]. The agreement is excellent on this scale with even the very weak oscillations being reproduced in both spectra. The spectral range in Fig. 4 is confined to the region of an observed resonance, analogous to the Cotton effect in homogeneous chiral media [13]. This resonance is expected to occur at a wavelength $\lambda_0 \sim n_{av}P$, where $P \sim (4.7/12.3)$ μm $\sim 0.38$ μm is the pitch of the chiral film and $n_{av} = (1/2)(n_{x'} + n_{z'})$ is the average of the two principal indices of refraction. Based on this simple formula, $n_{av}$ is predicted to be $n_{av} = 0.44/0.38 \sim 1.16$ [13].

In analyzing ($\tau_{pp}$, $\tau_{ps}$, $\tau_{sp}$) at normal incidence, one

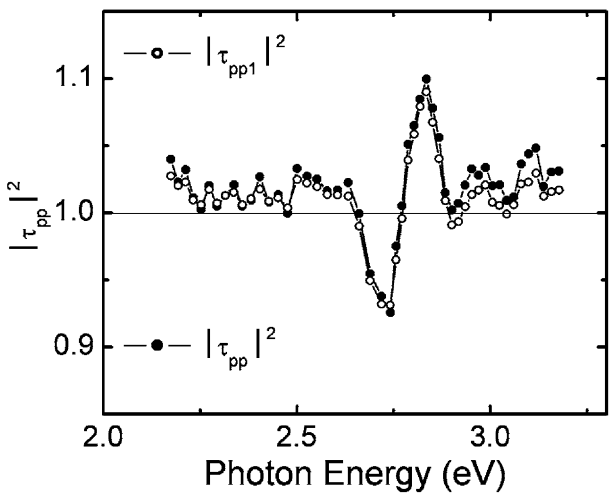


Fig. 4. Modulus-squared of $\tau_{pp}$ for the chiral STF from the LRB of the Mueller matrix with ULB normalization ($|\tau_{pp}|^2$: solid points) and from the ULB alone ($|\tau_{pp1}|^2$: open points).

can rotationally transform Berreman's equation [14] to derive a single transfer matrix for the chiral film [15]. This procedure is not straightforward at non-normal incidence [16], and in addition, cannot be applied to model non-uniformities with depth into the film. Thus, we have adopted a model usable under both such circumstances. In this model, a film of thickness $d$ and pitch $P$ is treated as a product of $N$ transfer matrices each for a uniaxial sublayer of thickness $\Delta d = d/N$. The azimuthal Euler angle $\phi$ is stepped from the surface ($j=1$) to the substrate ($j=N$) according to $\phi_j = \phi_0 + (N-j)\Delta\phi$, where $\phi_0$ is the value at the substrate interface and $\Delta\phi = (2\pi/N)(d/P)$ is the sublayer step.

Fig. 5 shows a comparison of two simulations in $\tau_{pp}^{re}$ using the single and multilayer transfer matrix approaches. The following parameters found to best fit the data (see, e.g. Fig. 4) are used in both simulations: $d=4.7$ μm, $P=0.382$ μm, $\theta=31°$, $n_{av}(\lambda_0)=1.192$, and $\Delta n(\lambda_0) = n_{z'}(\lambda_0) - n_{x'}(\lambda_0) = 0.066$. Dispersions in ($n_{x'}$, $n_{z'}$) are incorporated, but these are relatively weak and will not be described. We omit a linear void gradient—needed to reasonably fit the data—because it cannot be incorporated into the single layer simulation. The number of layers in the multilayer simulation is set at $N=3000$, yielding $\Delta d = 15.7$ Å and $\Delta\phi = 1.45°$. This level of discretization generates excellent agreement with the single layer simulation for $\tau_{pp}^{re}$, as shown in Fig. 5, as well as for the other amplitude transmission ratios. This result lends confidence in the multilayer approach, which is advantageous in solving a wider range of STF problems.

Rather than describing the application of our multilayer model in a structural analysis for the chiral STF (as for the chevron STF above), we demonstrate simulations of spectra collected in transmission at oblique incidence as in Ref. [17]. In our study, experimental Mueller matrices acquired (rapidly) vs. $\theta_i$ for the chiral STF can be used to deduce spectra in the optical rotation $\Delta Q$ and imposed ellipticity $\Delta\chi$. This is done by multiplying the incident ($i$) beam Stokes vector for linearly polarized light with tilt angle $Q_i = 0°$ and ellipticity angle $\chi_i = 0°$ by the Mueller matrix so as to extract the transmitted ($t$) beam Stokes vector and its angles $Q_t = \Delta Q$ and $\chi_t = \Delta\chi$. Alternatively, Mueller matrix measurement can be bypassed in favor of a high-speed transmitted beam Stokes vector measurement of the chiral STF using incident linearly polarized light [13].

The upper panel of Fig. 6 shows just such results. In these experiments, the resonance appearing near $\lambda_0 = 0.44$ μm at $\theta_i = 0°$ is found to shift to shorter $\lambda$ (and out of the spectral range) with increasing $\theta_i$. Interestingly, a second resonance enters the spectral range from the near infrared and also shifts to shorter $\lambda$ with increasing $\theta_i$. It is this second resonance whose $\Delta Q$ variation with $\theta_i$ is plotted in the top panel of Fig. 6. The corresponding results in the bottom panel are derived from the multilayer theory, using the same parameters listed above (again neglecting the void gradient, which has a negligible effect on the predicted $\lambda_0$). Overall excellent agreement is observed between the resonance positions from experiment and theory as shown in Fig. 7. The experimental spectra exhibit a much more gradual amplitude increase with $\theta_i$ in Fig. 6, however, and this is attributed to coherence loss as the optical path length increases.

The resonance positions, i.e. the peaks in $\Delta Q$, in Fig. 7, are consistent with simple Bragg theory such that to achieve resonance, the projection of $m$ pitches onto the propagation vector of the light wave must match the wavelength in the film. This condition is given by $\lambda_0 \sim mP(n_{av}^2 - \sin^2\theta_i)^{1/2}$ and the expressions for $m=(1, 2)$ are plotted in Fig. 7 (light lines). These results

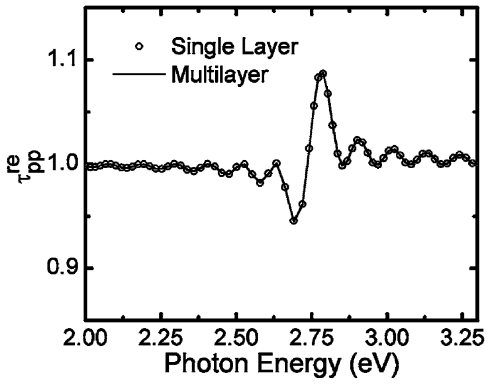


Fig. 5. A comparison of $\tau_{pp}^{re}$ spectra obtained in simulations of the chiral STF using single and multiple transfer matrices; the simulations incorporate structural and optical parameters that have been found to fit experimental data such as those of Fig. 4.

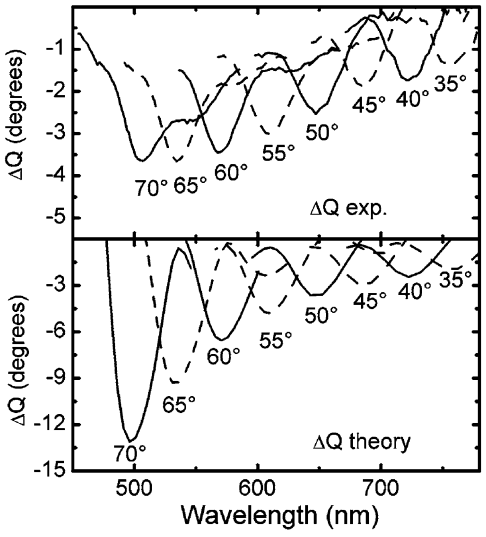


Fig. 6. Results from experiment top and multilayer theory for the optical rotation of an incident linearly polarized wave upon transmission through the chiral STF, at different incidence angles. The theory uses a parameter set that fits normal incidence data.

provide a clear experimental verification of Bragg resonance behavior for a chiral STF.

## 4. Summary

Dual rotating-compensator multichannel ellipsometry has been applied to measure spectra in the full Mueller matrices in reflection and transmission for sculptured thin films. Different methods of converting the Mueller matrix to the Jones matrix yield similar results, demonstrating the internal consistency of the former. Using multilayer theory to model the amplitude reflection and transmission ratios, we gain structural information such as thicknesses, Euler angles, chiral pitch, void fraction and its gradients, as well as optical information, namely, the spectra in the principal refractive indices. The Mueller matrix provides the transmitted polarization state for any incident state and demonstrates that the resonances in the optical rotation spectra of chiral thin films exhibit Bragg characteristics. Because of the high-speed nature of our Mueller matrix measurement, real time analysis of STFs during deposition will be explored in future research.

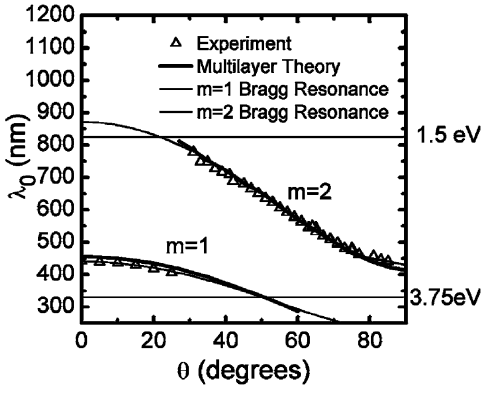


Fig. 7. Wavelength $\lambda_0$ of the resonance in $\Delta Q$ plotted vs. incidence angle for the experimental data (triangles) and multilayer theory of Fig. 6 (bold lines); also included is the result of a simple Bragg condition calculation in which the wavelength of light in the film is assumed to match the projection of *m* chiral pitches onto the light wave propagation vector (light lines).

## Acknowledgments

The authors acknowledge support of this research by NSF under Grant No. DMR-0137240 and by NREL under Subcontract AAD-9-18-668-09. The chiral STF was kindly provided by K. Robbie and M.J. Brett of the University of Alberta.

## References

[1] R. Messier, A. Lakhtakia, Mater. Res. Innov. 2 (1998) 217.
[2] H.J. Leamy, G.H. Gilmer, A.G. Dirks, in: E. Kaldis (Ed.), Current Topics in Materials Science, 6, North-Holland, Amsterdam, 1980, p. 309.
[3] T. Motohiro, Y. Taga, Appl. Opt. 28 (1989) 2466.
[4] K. Robbie, M.J. Brett, A. Lakhtakia, Nature 384 (1996) 616.
[5] R.W. Collins, J. Koh, J. Opt. Soc. Am. A 16 (1999) 1997.
[6] J. Lee, J. Koh, R.W. Collins, Rev. Sci. Instrum. 72 (2001) 1742.
[7] G.E. Jellison Jr, F.A. Modine, Appl. Opt. 36 (1997) 8190.
[8] R.M.A. Azzam, N.M. Bashara, Ellipsometry and Polarized Light, North-Holland, Amsterdam, 1977.
[9] U. Rossow, Thin Solid Films 313–314 (1998) 97.
[10] C. Chen, I. An, R.W. Collins, Thin Solid Films, doi: 10.1016/j.tsf.2003.11.217.
[11] C. Chen, I. An, G.M. Ferreira, N.J. Podraza, J.A. Zapien, R.W. Collins, doi: 10.1016/j.tsf.2003.11.191.
[12] D.E. Aspnes, Thin Solid Films 89 (1982) 249.
[13] P.I. Rovira, R.A. Yarussi, R.W. Collins, V.C. Venugopal, A. Lakhtakia, R. Messier, K. Robbie, M. Brett, Thin Solid Films 313–314 (1998) 373.
[14] D.W. Berreman, J. Opt. Soc. Am. 62 (1972) 502.
[15] M. Schubert, Phys. Rev. B 53 (1996) 4265.
[16] M. Schubert, C.M. Herzinger, Phys. Status Solidi (a) 188 (2001) 1563.
[17] M. Schubert, A. Kasic, T. Hoffmann, V. Gottschalch, J. Off, F. Scholz, E. Schubert, H. Neumann, I. Hodgkinson, M. Arnold, W. Dollase, C.M. Herzinger, Proc. SPIE 4806 (2002) 264.